ELSEVIER

International Journal of Heat and Fluid Flow 20 (1999) 581–591

International Journal of HEAT AND FLUID FLOW

www.elsevier.com/locate/ijhff

Predicting turbulent flow in a staggered tube bundle

J.K. Watterson [a,*], W.N. Dawes [b], A.M. Savill [b], A.J. White [b]

[a] *Department of Aeronautical Engineering, The Queen's University of Belfast, Belfast BT9 5AG, UK*
[b] *Department of Engineering, University of Cambridge, Cambridge, UK*

Received 10 December 1996; accepted 2 May 1999

Abstract

This paper presents the results of calculations performed for the turbulent, incompressible flow around a staggered array of tubes for which carefully obtained experimental results are available as part of an established ERCOFTAC-IAHR test case. The Reynolds-averaged Navier–Stokes equations are solved using a pressure-based finite volume algorithm, using collocated cell vertex store on an unstructured and adaptive mesh of tetrahedra. Turbulence closure is obtained with a truncated form of a low-Reynolds number k–ε model developed by Yang and Shih. The computational domain covers all seven rows of tubes used in the experimental study and periodic flow is allowed to develop naturally. The results of the computations are surprisingly good and compare favourably with results obtained by others using a wide range of alternative k–ε models for a single cylinder with periodic inflow and outflow boundaries on structured meshes.

Keywords: Turbulence models; CFD; Unstructured meshes

Notation

C_μ	turbulent viscosity constant of proportionality
f_μ	wall damping function
h_o	stagnation enthalpy per unit mass
$\underline{I}$	unit matrix
k	turbulence kinetic energy
P	turbulent kinetic energy production term
R	wall damping parameter (form of turbulence Reynolds number)
S,S_{ij}	modulus and component of strain rate tensor
T_t	turbulence time scale
$\underline{u}$	mean velocity vector
u', v'	turbulent velocity fluctuations
y^+	scaled wall normal distance
γ	ratio of specific heats
ε	turbulence kinetic energy dissipation rate
μ,μ_t	laminar and turbulent dynamic viscosity
ν	kinematic viscosity
ρ	density
$\underline{\tau}^R$	Reynolds stress tensor

1. Introduction

Many of the flows of interest to engineers involve either complex geometries or complex flow features, and often the two are found in combination. Still further complexity may arise if the flow also includes a mixture of incompressible and compressible flow sub-domains, such as the transonic primary gas path and essentially incompressible secondary air path which obtain in the case of turbomachinery blading with internal coolant passages. If computational methods are to be applied to the simulation of such flows it is essential to provide meshes of sufficient complexity and fineness to resolve the important features of the geometry and flow, and the computational technique may be required to simulate a wide range of Mach numbers. Conventional structured mesh algorithms can employ patched grids (Thomas et al., 1989) and embedded meshes (Ng, 1992) to provide the necessary mesh support; and if the simulation involves a wide range of Mach numbers, a pressure-based algorithm may be used (Shyy et al., 1992). Alternatively, the engineer may now take advantage of the powerful flexibility provided by the unstructured mesh finite volume approach (Jameson and Baker, 1987), which allows for the routine meshing of very complex geometries and adaptive mesh refinement on important flow features, although these new methods have generally been restricted to Mach numbers above approximately 0.3.

To extend the range of application of the unstructured mesh finite volume method to complex incompressible flows a pressure-based method has been developed (Watterson, 1994). The pressure-basis allows low-speed flows to be calculated, whilst retaining the use of unstructured meshes makes it possible to apply the method to very complex geometries. The low-Reynolds number model of Yang and Shih (1993) has been used because it avoids the need for a turbulent viscosity damping function based on wall normal distance: a length scale not easily obtained when using unstructured meshes. In order to test the low speed accuracy of the numerical method it has been applied to the turbulent, incompressible flow about a

* Corresponding author.
E-mail address: j.watterson@queens-belfast.ac.uk (J.K. Watterson)

0142-727X/99/$ - see front matter
PII: S0142-727X(99)00049-1

staggered bundle of tubes reported by Simonin and Barcouda (1988). This test case was used at the 2nd ERCOFTAC-IAHR Workshop on Refined Flow Modelling (Leschziner and Launder, 1993). This flow provides a challenging test case for both the numerical method and the turbulence model employed in the present work. The results of the calculations were reported briefly at the 3rd ERCOFTAC-IAHR Workshop on Refined Flow Modelling (Watterson et al., 1994) but are discussed and compared with both experimental and other model results in greater detail here.

2. Numerical method

The numerical method used in this work has been described in detail by Watterson (1994). The scheme is based upon a straightforward interpretation of the concept of a pressure correction method. However, whereas traditional pressure correction methods (e.g. Issa and Lockwood, 1977; Patankar, 1980) have employed velocity as the subject of the momentum equations, this method follows the example of Harlow and Amsden (1971) and McGuirk and Page (1990) by treating momentum as such. This results in a method not limited to low speed flows and good shock capturing properties. The algorithm employs collocated cell-vertex store in order to obviate the difficulties and disadvantages of implementing a non-collocated (staggered) mesh within the unstructured methodology. The convective fluxes are accumulated in the spatially centred fashion of Jameson and Baker (1987) rather than in an upwind manner, and artificial dissipation is added in order to control velocity-pressure decoupling and the shock capturing properties. The viscous fluxes are evaluated in the fashion of Mavriplis et al (1989). The whole scheme is integrated to steady state via explicit four stage Runge–Kutta time marching.

2.1. Governing equations

The numerical method solves discretisations of the continuity and Navier–Stokes equations:

$$\frac{\partial \rho}{\partial t} + \nabla \cdot \rho \underline{u} = 0, \tag{1}$$

$$\frac{\partial \rho \underline{u}}{\partial t} + \nabla \cdot (\rho \underline{u} \otimes \underline{u} + p\underline{I} - \underline{\tau}) = 0. \tag{2}$$

The full energy equation is not used in this work. Instead the flow is assumed to be isenthalpic, so that the energy equation reduces to

$$h_o = \frac{\gamma p}{(\gamma - 1)\rho} + \frac{1}{2} u_i u_i. \tag{3}$$

Pressure, density and temperature are further related through the equation of state. In the Reynolds-averaged form of the equations the viscous stress tensor, $\underline{\tau}$, comprises laminar, $\underline{\tau}^{\mathrm{l}}$, and turbulent, $\underline{\tau}^{\mathrm{R}}$, contributions whose tensor components are given by,

$$\tau^{\mathrm{l}}_{ij} = \mu \left(\partial_i u_j + \partial_j u_i - \frac{2}{3} \nabla \cdot \underline{u} \delta_{ij} \right) \tag{4}$$

and

$$\tau^{\mathrm{R}}_{ij} = \mu_{\mathrm{t}} \left(\partial_i u_j + \partial_j u_i - \frac{2}{3} \nabla \cdot \underline{u} \delta_{ij} \right) - \frac{2}{3} \rho k \delta_{ij}. \tag{5}$$

Closure is provided by the k–ε turbulence model.

$$\frac{\mathrm{D}k}{\mathrm{D}t} = \nabla \cdot \left(\left(\nu + \frac{\nu_{\mathrm{t}}}{\sigma_k} \right) \nabla k \right) + P - \varepsilon, \tag{6}$$

$$\frac{\mathrm{D}\varepsilon}{\mathrm{D}t} = \nabla \cdot \left(\left(\nu + \frac{\nu_{\mathrm{t}}}{\sigma_\varepsilon} \right) \nabla \varepsilon \right) + (C_{1\varepsilon} P - C_{2\varepsilon} \varepsilon) \frac{1}{T_{\mathrm{t}}} + C_\varepsilon \nu \nu_{\mathrm{t}} u_{i,jk} u_{i,jk}, \tag{7}$$

where the constants take their usual values, i.e. $\sigma_k = 1.0$, $\sigma_\varepsilon = 1.3$, $C_{1\varepsilon} = 1.44$ and $C_{2\varepsilon} = 1.92$. Yang and Shih (1993) choose $C_\varepsilon = 1.0$. The time scale T_{t} is described in Section 4.

2.2. Formulation of the pressure correction method

Suppose that time is discretised and let the superscript n refer to the conditions at the beginning of a cycle, n+1 to conditions at the end, and * to the intermediate conditions. Then consider an explicit, semi-discretisation of Eq. (2) with time step δt,

$$\frac{\rho \underline{u}^* - \rho \underline{u}^n}{\delta t} = -\nabla \cdot (\rho \underline{u} \otimes \underline{u})^n - \nabla p^n + \nabla \cdot \underline{\tau}^n. \tag{8}$$

The intermediate momentum field $\rho \underline{u}^*$ is obtained from the solution of Eq. (8). In general, $\rho \underline{u}^*$ will not satisfy the continuity equation. The final values of momentum and pressure may be sought by applying corrections, denoted $()'$,

$$\rho \underline{u}^{n+1} = \rho \underline{u}^* + \rho \underline{u}' \tag{9}$$

and

$$p^{n+1} = p^n + p'. \tag{10}$$

Since the values at the end of the cycle are to be solutions of the continuity and momentum equations, then,

$$\frac{\rho^{n+1} - \rho^n}{\delta t} + \nabla \cdot \rho \underline{u}^{n+1} = \frac{\rho'}{\delta t} + \nabla \cdot \rho \underline{u}^{n+1} = 0 \tag{11}$$

and

$$\frac{\rho \underline{u}^{n+1} - \rho \underline{u}^n}{\delta t} = -\nabla \cdot (\rho \underline{u} \otimes \underline{u})^n - \nabla p^{n+1} + \nabla \cdot \underline{\tau}^n. \tag{12}$$

Subtracting Eq. (8) from Eq. (12) and substituting Eqs. (9) and (10) gives the relationship between the pressure and momentum corrections,

$$\frac{\rho \underline{u}'}{\delta t} = \frac{\rho \underline{u}^{n+1} - \rho \underline{u}^*}{\delta t} = -\nabla p'. \tag{13}$$

Taking the divergence of Eq. (13) leads to

$$\frac{\nabla \cdot \rho \underline{u}^{n+1} - \nabla \cdot \rho \underline{u}^*}{\delta t} = -\nabla^2 p'. \tag{14}$$

The divergence of the intermediate field $\rho \underline{u}^*$ can be easily calculated

$$\nabla \cdot \rho \underline{u}^* = Q_{\mathrm{D}}. \tag{15}$$

Then substituting Eqs. (11) and (15) into Eq. (14) gives

$$\frac{\rho'}{\delta t} - \delta t \nabla^2 p' = -Q_{\mathrm{D}}. \tag{16}$$

The energy Eq. (3) can be used to relate the density change, ρ', to the pressure correction, assuming negligible effect from the corrected velocity field, i.e.

$$\rho' = \frac{\gamma p'}{(\gamma - 1)\left(h_o - \frac{1}{2} u_i u_i\right)} \tag{17}$$

or

$$\rho' = S_\rho p', \tag{18}$$

where

$$S_\rho = \frac{\gamma}{(\gamma - 1)\left(h_o - \frac{1}{2} u_i u_i\right)}. \tag{19}$$

Substituting Eq. (17) into Eq. (16) gives

$$\frac{S_\rho}{\delta t}p' - \delta t \nabla^2 p' = -Q_D. \tag{20}$$

Eq. (20) is the Poisson equation for the pressure correction, solution of which provides the correction ρ' which is substituted into Eq. (13) to give the correction to the momentum field.

2.3. Implementation of the algorithm

When the solution domain is discretised, implementation of a scheme to solve the above equations requires the following steps. The momentum difference equations are solved to obtain the intermediate momentum field; the momentum residuals, i.e. the right hand side of Eq. (6), are obtained by a nominally second order spatially centred finite volume method. The divergence defect, Q_D, is then evaluated, also by the spatially centred finite volume method, and the Poisson equation for the pressure correction is solved. The corrections can then be calculated and applied; under-relaxation is employed at this stage. Finally the usual boundary conditions are applied. These steps are repeated to convergence. The difference equations for k and ε are cycled to convergence in parallel with the momentum equations.

2.4. Artificial dissipation

Artificial dissipation is required to control the velocity–pressure decoupling of the solution and shock capture. It is particularly important that the artificial dissipation operators are constructed in such a way that they do not corrupt the accuracy of the scheme. The generally accepted practice is to employ an adaptive mix of second and fourth difference smoothing operators – in the vicinity of shocks the second difference smoothing is switched on and the fourth difference is switched off. Of course, for low speed flow calculations such as those reported here, only the fourth difference smoothing is used. In this work, the artificial dissipation operator of Mavriplis (1990) was used.

3. Mesh generation

The meshes used for the present calculations were generated using an advancing front method. The mesh generator first develops a two-dimensional mesh in the plane of interest; this is then expanded into the third dimension and the resulting prismatic elements are divided into tetrahedra. For the results reported here, the two-dimensional mesh was expanded to be initially only three nodes deep; the solutions which are presented have been taken from slices through the mid-planes of the domain. Unfortunately, mesh refinement for such two-dimensional calculations is inefficient because the refinement process is three-dimensional and generates excessive extra mesh in the third dimension. However, numerical experiments have shown that the use of solution adaptive mesh refinement is still able to provide cpu savings under these circumstances (Watterson et al., 1998).

4. Turbulence model

The k–ε turbulence model developed by Yang and Shih (1993) has several features that make it ideally suited for implementation on the unstructured meshes used in this work. First, the model employs the standard model constants, and reduces to the standard k–ε model away from the wall. Second, the model uses a turbulent time scale that has the Kolmogorov time scale as its lower bound; thus the wall singularity is removed and the model can be integrated to the wall without recourse to a pseudo-dissipation variable. Finally, the independent variable in the eddy viscosity damping function is evaluated from the local strain rates of the flow rather than the y^+ value or wall normal distance. These latter parameters are of ambiguous value in separated or complex three-dimensional flows, and are, moreover, very difficult to evaluate on unstructured meshes. The use of local strain rate also provides a necessary additional strain sensitivity similar to that which appears in the alternative RNG k–ε model and other non-linear k–ε schemes applied to the same test case (see Leschziner and Launder 1993).

Although the model is best described by its developers, a basic description will be given here. The turbulent viscosity μ_t is given by,

$$\mu_t = \rho C_\mu f_\mu k T_t, \tag{21}$$

where T_t is the time scale for turbulent flows and is written,

$$T_t = \frac{k}{\varepsilon} + \left(\frac{\mu}{\rho\varepsilon}\right)^{1/2}. \tag{22}$$

The first term on the right hand side of Eq. (22) is the conventional time scale; the second term is the Kolmogorov time scale. Away from the wall, the first term is very much larger than the second, but as the wall is approached the first term tends to zero because of the wall boundary condition on k, and T_t tends toward the Kolmogorov time scale. Since the wall value of the time scale is non-zero, the boundary condition for the dissipation equation is well behaved. The damping function, f_μ, takes account of the effect of the wall on the eddy viscosity. It is given by,

$$f_\mu = \left[1 - \exp\left(-a_1 R - a_2 R^2 - a_3 R^3\right)\right]^{1/2}, \tag{23}$$

where the parameter R is defined as,

$$R = \frac{\rho k}{S\mu} \tag{24}$$

and S is the modulus of the strain rate tensor, $S_{ij}\underline{e}_i\underline{e}_j$, of the mean velocity field,

$$S = \left(2S_{ij}S_{ij}\right)^{1/2}. \tag{25}$$

The coefficients in Eq. (23) are constants given by Yang and Shih as $a_1 = 3 \times 10^{-4}$, $a_2 = 6 \times 10^{-5}$ and $a_3 = 2 \times 10^{-6}$. The parameter R was chosen as the independent variable because turbulent channel flow calculations showed that it increases monotonically with y^+ near the wall region. Since the tensor components S_{ij} must be evaluated to obtain the turbulent kinetic energy production term the calculation of R requires little extra computation.

The model of Yang and Shih also includes the second-mean velocity derivative term $C_\varepsilon \nu \nu_t u_{i,jk} u_{i,jk}$ in the dissipation equation. This is equivalent to the additional E term which appears in some other low Re formulations and which models the production of ε in the near wall region by the gradients in ε. Yang and Shih chose a value of 1.0 for the constant C_ε based on the model performance in turbulent channel flows. This is half the value used in similar low Reynolds number k–ε models. However, significant computational effort is required to calculate this term when working with three-dimensional unstructured meshes, and it has been dropped from the model. For this reason, the model used in this work is best described as a truncated version of the Yang and Shih model. The influence of this decision will be discussed in the next section.

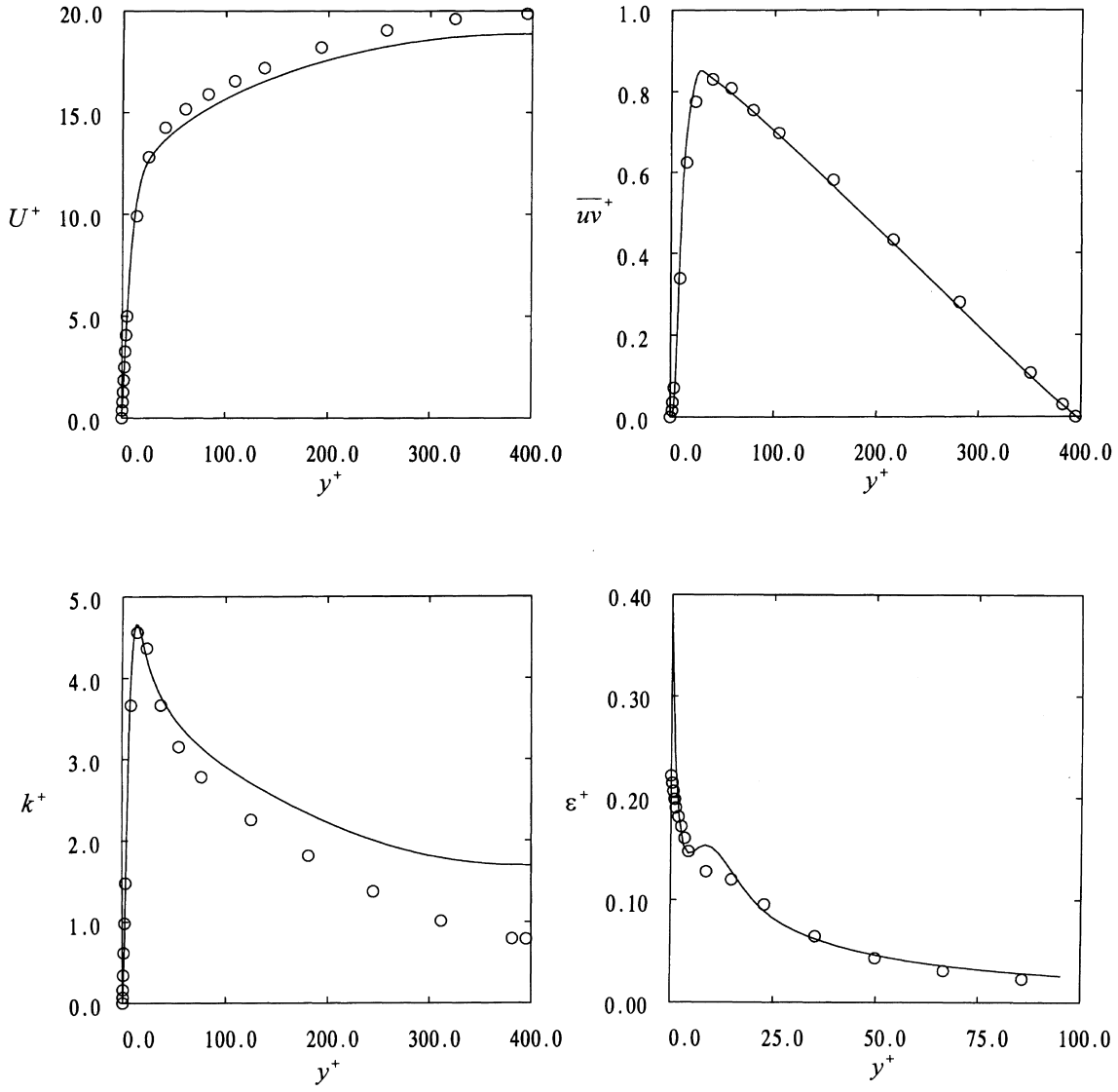

Fig. 1. Turbulent Channel flow at $Re_t = 395$ ooo DNS (Yang and Shih, 1993); ——— Calculation.

The wall boundary conditions for the Yang and Shih model have been retained. k is set to zero on solid walls. The wall boundary condition for ε is

$$\varepsilon_w = 2\nu\left(\frac{d\sqrt{k}}{dy}\right)^2. \tag{26}$$

5. Results and discussion

5.1. Fully developed channel flow

The numerical method has been tested against fully developed turbulent channel flow. The Reynolds number of the flow is 395, based on the friction velocity and the channel depth. The full span of the channel was meshed with 99 points. 11 points were used in the streamwise direction and the through-flow boundaries were made periodic. In Fig. 1 the solution is compared with DNS data of Kim et al. (1987). The prediction is satisfactory, though several shortcomings ought to be mentioned. The centreline velocity is under predicted by 5%. The peak value of k is well reproduced, but towards the centreline the values are over predicted. The wall value of ε is too large, and this may be the result of the second-mean velocity derivative term neglected in the constitutive equation for dissipation rate. However, the profile of ε does follow the DNS results quite well, albeit showing a tendency to over prediction away from the wall.

5.2. Tube bundle geometry

The experiments performed by Simonin and Barcouda (1988) and the measurements released through the 2nd ER-COFTAC–IAHR Workshop on Refined Flow Modelling (Leschziner and Launder 1993) have been used as the basis of the calculations reported here. The experimental test section consisted of seven horizontal, staggered rows of 21.7 mm diameter rods, across which water flowed at an average velocity of 1.06 ms^{-1}, giving a Reynolds number, based on the rod diameter, of 18×10^3. This arrangement is similar to that of a heat exchanger, but for the test case heat transfer was not considered. LDA measurements were taken in the vicinity of the fifth tube where the flow was observed to have become

periodic, and experimental data along five traverse planes was released through the ERCOFTAC–IAHR workshop.

Assuming fully axially periodic, steady flow (which the experiments showed to have been established between the 4th and 5th rows) the computational domain could have been restricted to the single flow passage shown in Fig. 2, as most other flow modellers have done. However, for this work the full cascade of seven tubes was chosen as the computational domain, and this, together with the planes from which calculated values were extracted for comparison with measurements is shown in Fig. 3. The point O is in the centre of the quadrangle of adjacent tubes. Results were extracted at: $x = X_i$ along AO; $x = X_r$ along BC; $x = X_b$ along DE; $y = Y_{\text{wake}}$ along FO; and $y = Y_{\text{impact}}$ along OG. The upper and lower boundaries were specified as periodic. The plane $x = X_i$ was chosen as the periodic inflow/outflow boundary for many of the structured mesh computations reported by Leschziner and Launder (1993).

The visualisation planes from the original and final meshes are shown in Figs. 4(a) and (b), respectively. The initial mesh contained 17 255 cells and 4605 nodes, with 1535 nodes in the visualisation plane. After a solution had been obtained on the initial mesh, the cells adjacent to the surfaces of all the tubes and in the region from upstream of the fourth tube to downstream of the fifth tube were refined. A solution was obtained on this mesh and the final mesh was created by refining again the cells adjacent to the surfaces of the tubes, although this refinement was restricted to the region from 60% chord of the third tube to 35% chord of the sixth tube. It is estimated that the y^+ value of mesh at the 12 O'clock position on the fourth tube is about 15.

The final mesh contained 181 257 cells and 38 586 nodes, with 5702 nodes in the visualisation plane, i.e. a tenfold increase in the number of cells and eight times as many nodes (but less then a fourfold increase in the number of nodes in the visualisation plane). Two levels of uniform two-dimensional

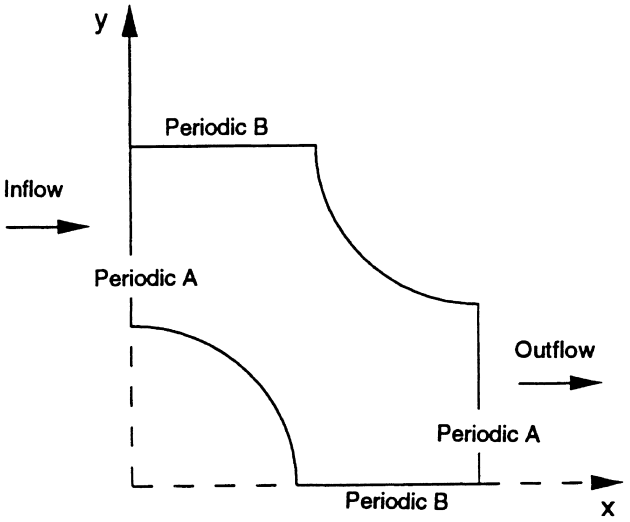

Fig. 2. Restricted domain for periodic tube bundle flow.

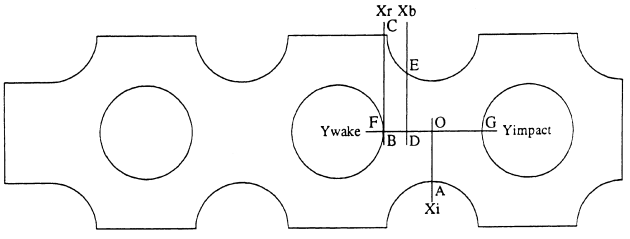

Fig. 3. Full domain for tube bundle flow, showing positions at which results were extracted.

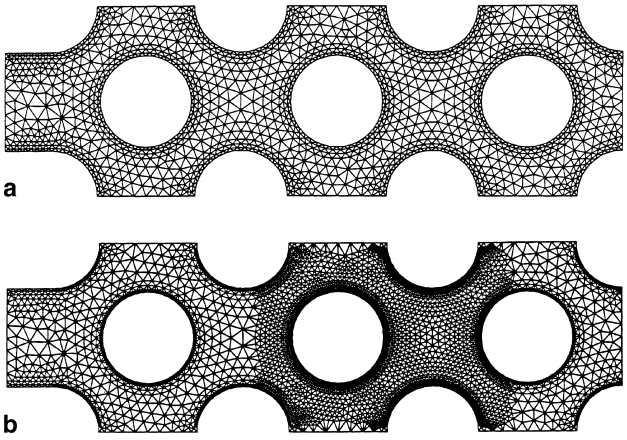

Fig. 4. (a) Initial mesh; (b) final mesh after two levels of adaptive mesh refinement.

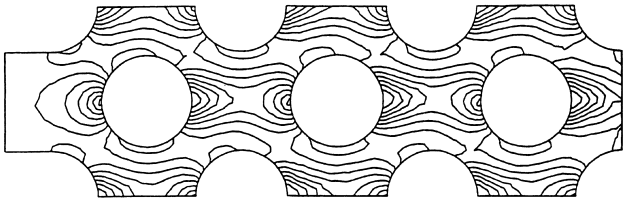

Fig. 5. Contours of velocity predicted on initial mesh.

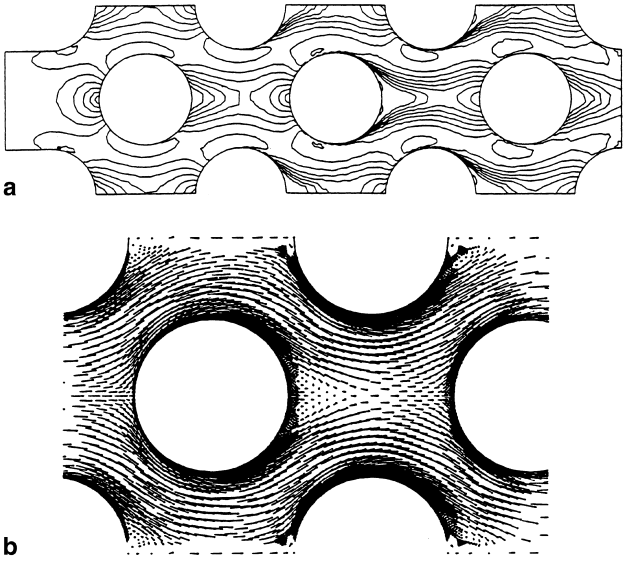

Fig. 6. (a) Contours of velocity predicted on final mesh; (b) velocity vectors predicted on final mesh in region of most intense mesh refinement.

refinement would have resulted in a sixteen fold increase in the numbers of cells and nodes. Thus, because mesh refinement was deliberately focused on the region of the solution domain where axially periodic flow was expected to be established and from which the results would be extracted, a saving of between 37% and 50% in mesh required was obtained.

5.3. Prediction of through flow topology

For reference, the solution on the initial mesh is shown in Fig. 5, which shows the velocity contours. Periodic flow is established in the region of the fourth and fifth tubes and the flow is largely symmetric (there is a small periodic asymmetry). The peak velocity is approximately 16 m s^{-1}. However, the

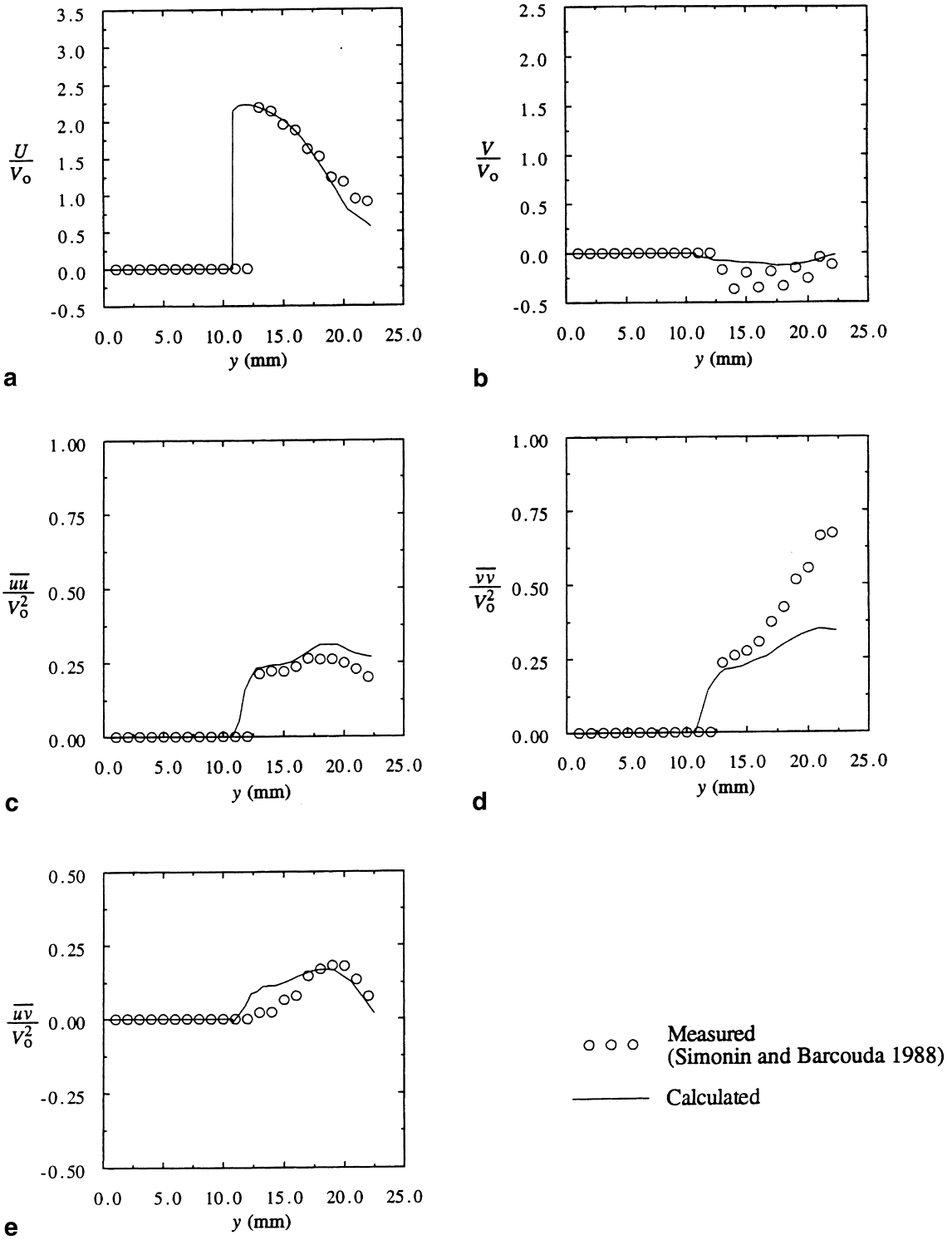

Fig. 7. Results extracted at $x = X_i$.

velocity vectors (not shown) indicate that the flow remains attached to the trailing-edge stagnation points on the tubes.

The solution on the final mesh is shown in Fig. 6. As Fig 6(a) shows, the velocity contours are now more symmetric than those obtained on the initial mesh. The flow about the fourth and fifth tubes is periodic. Again the peak velocity is 16 ms^{-1}. The velocity vectors are shown in Fig. 6(a). A region of flow reversal is now seen behind the third, fourth and fifth tubes, where the cells adjacent to the aft surfaces have been refined twice.

Comparing Figs. 5 and 6 it may be seen that the initial mesh is sufficient to predict the periodicity of the flow. However, a threshold level of mesh support is required to resolve the boundary layers without which the separation zone is not predicted properly, if at all. Accurate prediction of the separation zone is vital because its extent effectively defines the

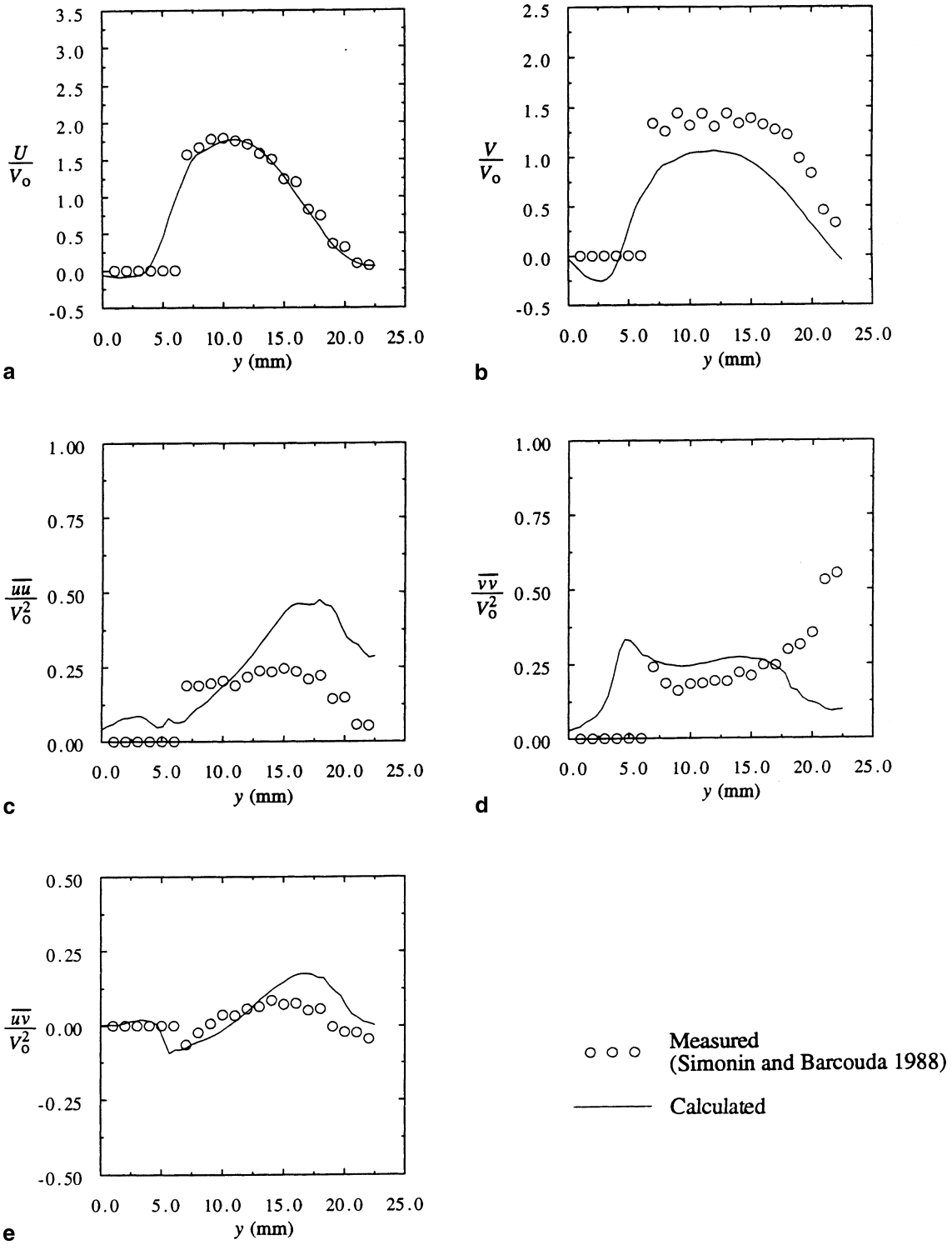

Fig. 8. Results extracted at $x = X_r$.

through-flow geometry. Moreover, the state of the boundary layers would be of critical importance if heat transfer predictions were to be performed.

5.4. Mean flow predictions

Mean flow values and Reynolds stresses have been extracted from the solution on the final mesh at the five stations described above and shown in Fig. 3. These have been plotted together with the measurements of Simonin and Barcouda (1988), and the results are presented in Figs. 7–11. Because the calculation and the experiment were performed with different fluids, a reference velocity was chosen that gave the best agreement between the calculated and measured axial velocity profiles at the traverse plane $x = X_i$ – see Fig. 7 (a). A reference velocity of 7.5 m s^{-1} was chosen, and Fig. 7(a) indicates that

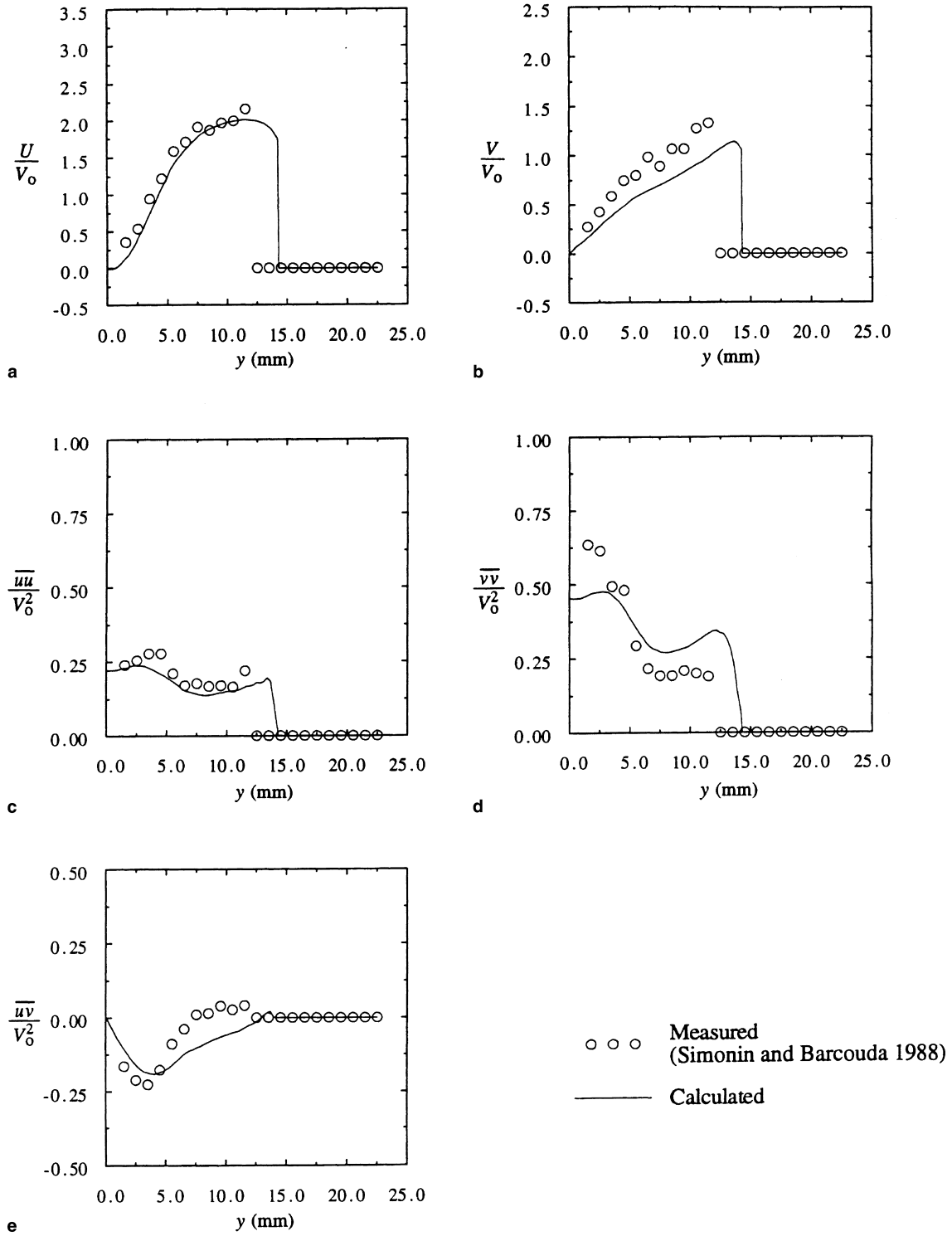

Fig. 9. Results extracted at $x = X_b$.

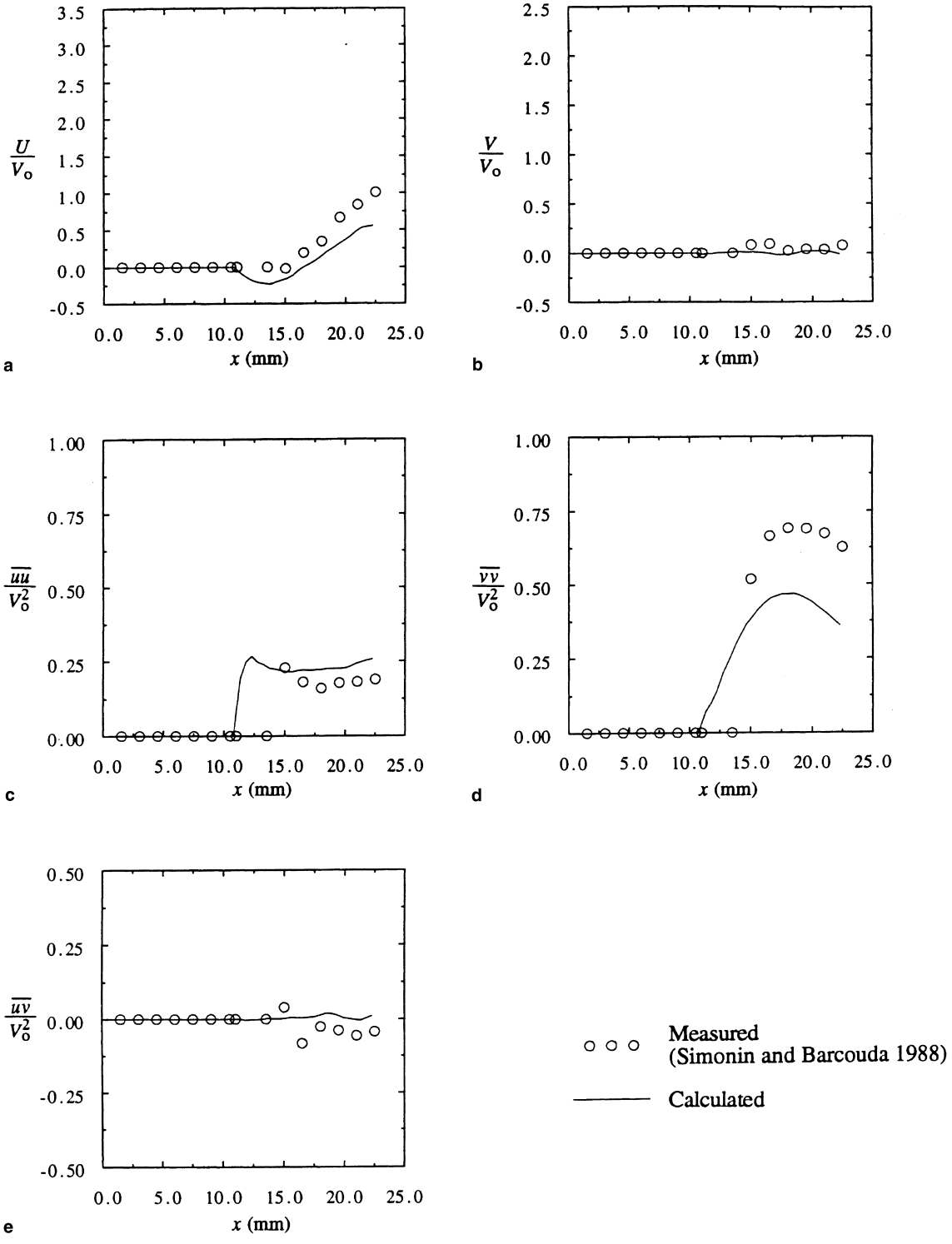

Fig. 10. Results extracted at $y = Y_{wake}$.

the mean axial "inflow" velocity was 12.3 m s^{-1} giving a Reynolds number of 21×10^3, slightly higher than the experimental value of 18×10^3.

The axial and transverse velocity profiles at $x = X_r$ are presented in Fig. 8(a) and (b), respectively. The transverse extent of the separation region may be slightly under predicted, but the magnitude of the recirculation region is close to the expected level and there is some uncertainty as to how close to the solid walls the LDA measurements were taken: zero velocity values being specified both within solid surfaces and in flow regions close to these which could not be accessed by the measuring equipment (cf. Fig. 7(a)). Fig. 9(a) and (b) show the axial and transverse velocity profiles at $x = X_b$. Again the axial velocity profile is well predicted, but the magnitude of the transverse velocity is underestimated. Overall the calculated mean flow values compare well with the measurements. In

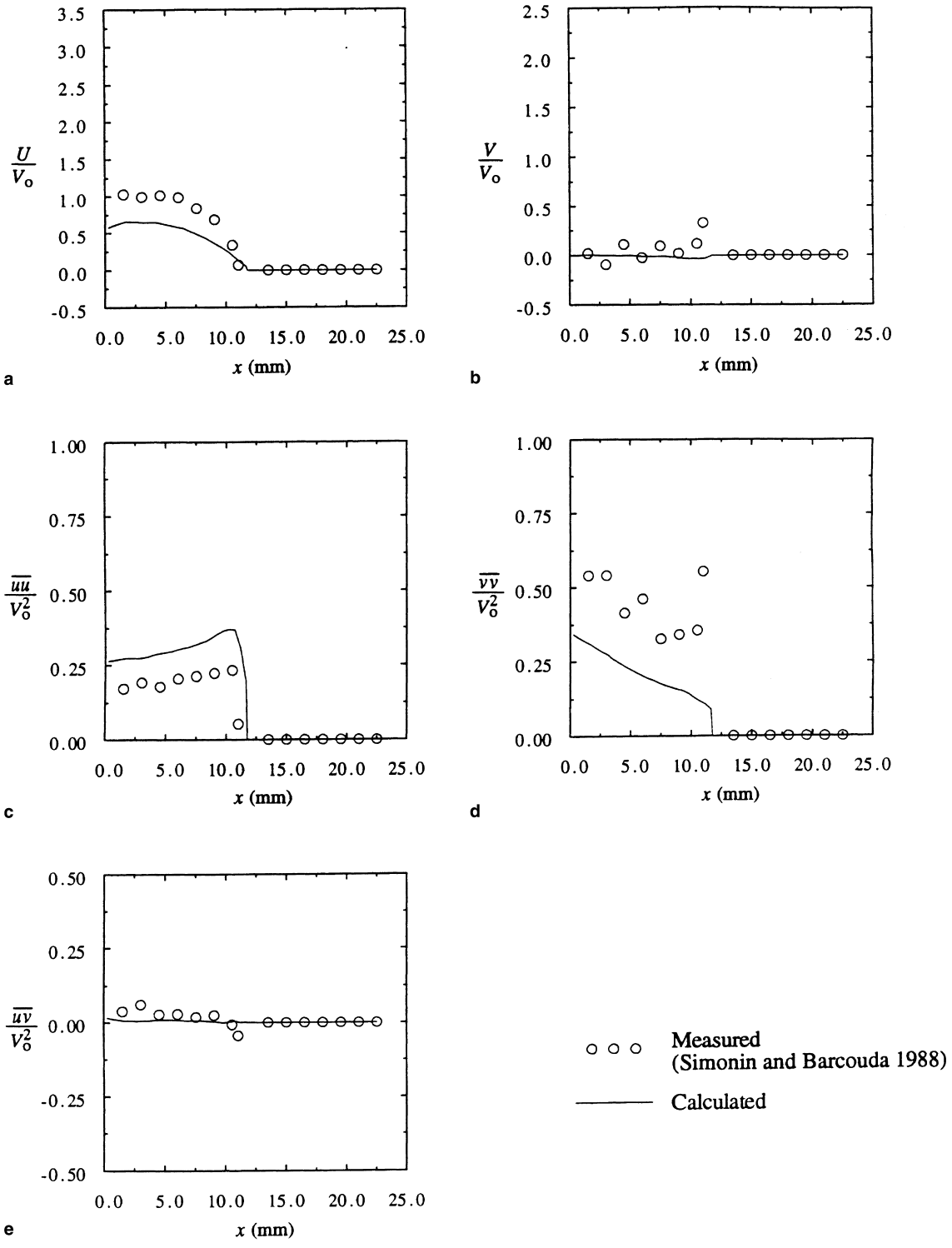

Fig. 11. Results extracted at $y = Y_{\text{impact}}$.

common with most of the models presented at the 2nd ERCOFTAC-IAHR Workshop on Refined Flow Modelling (Leschziner and Launder, 1993) the axial velocity variations in the wake (accelerating) and impact (decelerating) regions, Figs. 10(a) and 11(a), respectively, are under predicted, and the axial extent of the separation zone appears to be over predicted. These deficiencies point to the need for more selective mesh refinement in both the impingement and recirculation regions. These predictions proved to be better than some initial results obtained with the same code using the turbulence Reynolds number based Dawes low *Re* k–εmodel (Dawes, 1993) on a mesh with only half the resolution of the present fine mesh, which were in turn equivalent to the best (Launder-Sharma) low *Re* k–ε model predictions reported at the 2nd ERCOFTAC-IAHR workshop. However, of the other strain dependent schemes which have so far been applied to this test case both

the Kato–Launder and RNG forms of the k–ε model considerably over predict the extent of the separation region behind the tubes. This is a serious deficiency and highlights a major achievement of the present scheme, since the extent of the separation zones effectively defines the geometry for the through flow. The Kato–Launder irrotational strain correction appears to need further calibration for the type of flow curvatures experienced by this through flow; while the RNG k–ε model, which has been widely shown to produce excellent predictions of separation at a back step seems far less successful when the separation point is not fixed.

5.5. Reynolds stress predictions

Predicted profiles of the Reynolds stresses are included for completeness but will not be discussed in detail as it is recognised that either a non-isotropic, non-linear k–ε or a full Reynolds stress transport approach is required to capture the full turbulence anisotropy effects. Generally, the magnitudes and trends of the turbulence quantities are predicted quite well. However, there is a clear discrepancy between the measurements and predictions in the cross flow variations of the $\overline{v'v'}$ normal stress in the region $y = 15$–20 mm (Figs. 7–9) and in the streamwise variations both upstream and downstream of the tubes (Figs. 10(d) and 11(d) respectively). In contrast the $\overline{u'u'}$ normal stress distribution is well predicted, with the exception of the cross flow variation at the base of the tube (Fig. 8(c)), and overall the Reynolds stress predictions compare favourably with those reported for other k–ε models (Leschziner and Launder, 1993). In particular the $\overline{u'v'}$ Reynolds shear stress variations have been well predicted everywhere in both magnitude and trend; this explains why the model has been able to do such a good job of predicting the mean flow field even though it cannot describe the anisotropy of the Reynolds stress field correctly. Even for $\overline{u'v'}$ there are discrepancies, as for example in the cross flow variation shown in Fig. 9(e) where it appears that the numerical method has not captured the concentration of the Reynolds shear stress in the inner portion of the separated flow region.

6. Conclusions

The calculation of low speed, turbulent flow in an array of staggered tubes has been presented. Both the predicted mean values and Reynolds stresses show encouraging agreement with experimental measurements. The implementation of the turbulence model appears to be effective, and the results compare favourably with those obtained by structured mesh solvers designed specifically for incompressible flow and reported at the 2nd and 3rd ERCOFTAC–IAHR workshops (Leschziner and Launder, 1993 and Hanjalic and Hadzic, 1998). Overall, the agreement between the predictions and experiments is encouraging and this validation case gives confidence in the low speed, viscous capability of the solver and the suitability of the Yang and Shih low Re k–ε turbulence model for separating flows in complex, confined geometries. The benefits of adaptive mesh refinement have also been illustrated, with up to a 50% saving in mesh required for resolution obtained.

Acknowledgements

Much of the work presented here was performed with the financial assistance of a postgraduate award from the Department of Education for Northern Ireland and of a grant from the Ford of Britain Fund administered by the Cambridge University Engineering Department.

References

Dawes, W.N., 1993. The practical application of solution-adaption to the numerical solution of complex turbomachinery problems. Progress in Aerospace Sciences 29, 221–269.

Hanjalic, K., Hadzic, I., 1998. 3rd ERCOFTAC–IAHR workshop on refined flow modelling: turbulent flow and heat transfer in a subchannel of a staggered tube bundle. T.U. Delft Technical Report.

Harlow, F.H., Amsden, A.A., 1971. A numerical fluid dynamics calculation method for all flow speeds. J. Comp. Phys. 8, 197–213.

Issa, R.I., Lockwood, F.C., 1977. On the prediction of two-dimensional supersonic viscous interactions near walls. AIAA J. 15 (2), 182–188.

Jameson, A., Baker, T.J., 1987. Improvements to the aircraft Euler method. In: AIAA 25th Aerospace Science Meeting, Paper 87-0452.

Kim, J., Moin, P., Moser, R., 1987. Turbulent statistics in fully developed channel flow at low reynolds number. J. Fluid Mech. 177, 133–166.

Leschziner, M. A., Launder, B. E., 1993. Round normally impinging turbulent jet and turbulent flow through tube bank sub-channel. In: Proceedings of 2nd ERCOFTAC–IAHR workshop on refined flow modelling, UMIST.

Mavriplis, D.J., 1990. Accurate multigrid solution of the euler equations on unstructured and adaptive meshes. AIAA J. 28 (2), 213–221.

Mavriplis, D.J., Jameson, A., Martinelli, L., 1989. Multigrid solution of the Navier–Stokes equations on triangular meshes. NASA CR-181786, ICASE Rep. No. 89-11.

McGuirk, J.J., Page, G.J., 1990. Shock capturing using a pressure-correction method. AIAA J. 28 (10), 1751–1757.

Ng, Y.-K., 1992. A high-resolution coupled parabolic/elliptic Navier–Stokes solver for turbomachinery flows. Ph.D. thesis, Whittle Laboratory, University of Cambridge.

Patankar, S.V., 1980. Numerical Heat Transfer and Fluid Flow. Hemisphere, Washington, DC.

Shyy, W., Chen, M.-H., Sun, C-S., 1992. Pressure-based multigrid algorithm for flow at all speeds. AIAA J. 30 (11), 2660–2669.

Simonin, D., Barcouda, M., 1988. Measurements and predictions of turbulent flow entering a staggered tube bundle. EDF report H-44/88.25.

Thomas, J.L., Walters, R.W., Reu, T., Ghaffari, F., Weston, R.P., Luckring, J.M., 1989. A patched-grid algorithm for complex configurations directed towards the F-18 Aircraft. AIAA 27th Aerospace Science Meeting Paper 89-0121.

Watterson, J.K., 1994. A pressure-based flow solver for the three-dimensional Navier–Stokes equations on unstructured and adaptive meshes. In: 25th AIAA Fluid Dynamics Conference, Paper 94-2358.

Watterson, J.K., Dawes, W.N., Savill, A.M., White, A.J., 1994. Turbulent flow in a staggered bundle of cylinders without heat transfer. In: 3rd ERCOFTAC-IAHR Workshop on Refined Flow Modelling, Lisbon.

Watterson, J.K., Connell, I.J., Savill, A.M., Dawes, W.N., 1998. A solution adaptive mesh procedure for predicting confined explosions. Int. J. Numer. Meth. Fluids 26, 235–247.

Yang, Z., Shih, T.H., 1993. A k–ε model for turbulent and transitional boundary layers. In: So, R.M.C., Speziale, C.G., Launder, B.M. (Eds.), Near Wall Turbulent Flows. Elsevier, Amsterdam, pp. 165–176.